



Electronic transition and electrical transport properties of delafossite CuCr_{1-x}Mg_xO₂ (0x12%) films prepared by the sol-gel method: A composition dependence study

M. J. Han, Z. H. Duan, J. Z. Zhang, S. Zhang, Y. W. Li, Z. G. Hu, and J. H. Chu

Citation: *Journal of Applied Physics* **114**, 163526 (2013); doi: 10.1063/1.4827856

View online: <http://dx.doi.org/10.1063/1.4827856>

View Table of Contents: <http://scitation.aip.org/content/aip/journal/jap/114/16?ver=pdfcov>

Published by the [AIP Publishing](#)



www.goodfellowusa.com

Goodfellow
metals • ceramics • polymers
composites • compounds • glasses

Save 5% • Buy online
70,000 products • Fast shipping

Electronic transition and electrical transport properties of delafossite CuCr_{1-x}Mg_xO₂ (0 ≤ x ≤ 12%) films prepared by the sol-gel method: A composition dependence study

M. J. Han (韩美杰), Z. H. Duan (段志华), J. Z. Zhang (张金中), S. Zhang (张思), Y. W. Li (李亚巍), Z. G. Hu (胡志高),^{a)} and J. H. Chu (褚君浩)

Key Laboratory of Polar Materials and Devices, Ministry of Education, Department of Electronic Engineering, East China Normal University, Shanghai 200241, China

(Received 28 November 2012; accepted 15 October 2013; published online 31 October 2013)

Highly transparent CuCr_{1-x}Mg_xO₂ (0 ≤ x ≤ 12%) films were prepared on (001) sapphire substrates by sol-gel method. The microstructure, phonon modes, optical band gap, and electrical transport properties have been systematically discussed. It was found that Mg-doping improved the crystal quality and enhanced the (00l) preferred orientation. The spectral transmittance of films approaches about 70%–75% in the visible-near-infrared wavelength region. With increasing Mg-composition, the optical band gap first declines and climbs up due to the band gap renormalization and Burstein-Moss effect. The direct and indirect band gaps of CuCr_{0.94}Mg_{0.06}O₂ film are 3.00 and 2.56 eV, respectively. In addition, it shows a crossover from the thermal activation behavior to that of three-dimensional variable range hopping from temperature-dependent electrical conductivity. The crossover temperature decreases with increasing Mg-doping composition, which can be ascribed to the change of spin-charge coupling between the hole and the local spin at Cr site. It should be noted that the electrical conductivity of CuCr_{1-x}Mg_xO₂ films becomes larger with increasing x value. The highest electrical conductivity of 3.85 S cm⁻¹ at room temperature for x = 12% is four-order magnitude larger than that (8.81 × 10⁻⁴ S cm⁻¹) for pure CuCrO₂ film. The high spectral transmittance and larger conductivity indicate that Mg-doped CuCrO₂ films are promising for optoelectronic device applications. © 2013 AIP Publishing LLC. [<http://dx.doi.org/10.1063/1.4827856>]

I. INTRODUCTION

Transparent conductive oxides (TCOs) are technologically important materials due to their functional combination of optical transparency and electrical conductivity. They are widely used as transparent electrodes in flat panel displays, touch panels, and solar cells.^{1–3} Whereas most of the well-known TCOs such as In₂O₃:Sn,⁴ ZnO:Al,⁵ and SnO₂:F (Ref. 6) are n-type semiconductors. Applications where TCOs work as transparent electronic devices require both n-type and p-type transparent conductive materials. For example, the combination of two type transparent conductors in the form of p-n junction can work as the light-emitting diodes or functional windows.⁷ The CuMO₂ delafossite family, where M = Al, Ga, In, or Cr, is attracting attention because it is stable and prototype p-type wide band transparent semiconductor without doping. The interest in p-type CuAlO₂ materials has been increased since p-type CuAlO₂ films have been successfully fabricated.⁸ Subsequently, the CuCrO₂ material has drawn increasing attention due to its lower synthesis temperature and better thermal stability, as compared with other delafossite materials. Although the delafossite compounds CuMO₂ (M = Al, Ga) are isostructural with the CuCrO₂ compound, the synthesis temperature of CuMO₂ (M = Al, Ga) films is about 900 °C.^{9,10} In contrast, the synthesis temperature of the CuCrO₂ film is only

about 600 °C.¹¹ In addition, the phase stability and thermal behavior of CuFeO₂ and CuCrO₂ delafossite compounds were studied by Lalanne *et al.* under the air atmosphere up to 1000 °C.¹² The CuFeO₂ compound is oxidized into the spinel (CuFe₂O₄) and copper monoxide (CuO) phases, whereas the CuCrO₂ is thermally stable. Actually, soaking CuCrO₂ in oxygen above 1200 °C produced CuCr₂O₄, so that the CuCrO₂ can be used as the high temperature oxidation resistant material. Therefore, it is necessary for the CuCrO₂ system to understand electronic band structures in both TCOs and high temperature application fields.

In delafossite CuCrO₂ compound, the structure can be visualized as consisting of two alternate layers: a planar layer of Cu cation in a triangular pattern and a CrO₂ layer with Cr³⁺-centered edge-sharing octahedra. Each Cu atom is linearly coordinated with two oxygen atoms to form an O-Cu-O dumbbell unit placed parallel to the c-axis.¹³ The crystal structure of CuCrO₂ compound is described by a rhombohedral spatial group R̄3m. There are only four atoms (one Cu, one Cr, and two O atoms) in the primitive rhombohedral cell. The hybridization of Cu 3d¹⁰ energy levels in the close energy proximity with O 2p levels increases energy of the valence band maximum and delocalizes hole state to form an intrinsic p-type semiconductor. For CuScO₂ and CuYO₂ compounds, intercalation with oxygen to form CuMO_{2+x} phases will improve their conductivity.¹⁴ However, it is difficult for CuCrO₂ compound because of the smaller ionic radius of Cr (0.615 Å).¹⁵ Therefore, the intrinsic resistance of the CuCrO₂ films is too large to be suitable for the practical

^{a)}Author to whom correspondence should be addressed. Electronic mail: zghu@ee.ecnu.edu.cn. Tel.: +86-21-54345150. Fax: +86-21-54345119.

application material/device.¹⁶ Fortunately, it is well known that doping the trivalent metal site with a divalent dopant significantly improves the conductivity of CuCrO₂ material. For example, Nagarajan *et al.* reported that the conductivity of CuCrO₂ bulk material increased approximately three orders of magnitude by Mg-doping, and the best *p*-type conductivity is 220 S cm⁻¹ for the CuCr_{0.95}Mg_{0.05}O₂ film prepared by radio frequency sputtering.¹⁷ It is larger than those of Ca-doped CuYO₂ and Mg-doped CuScO₂ films, and much larger than those of CuAl_{1-x}Mg_xO₂ films (4×10^{-4} S cm⁻¹) and CuIn_{1-x}Ca_xO₂ films (2.8×10^{-3} S cm⁻¹).^{18,19}

However, the transparency reported by Nagarajan *et al.* was about 30% in the visible range for the CuCr_{0.95}Mg_{0.05}O₂ film with 250 nm thickness. After annealing at 900 °C for about 2.5 min, the transparency can be increased to about 40%, but the conductivity is rapidly decreased to about 1 S cm⁻¹.¹⁷ The low transparency and weak electrical stability limited the applications of the CuCr_{1-x}Mg_xO₂ films. Bywalez *et al.*¹¹ also studied Mg-doping CuCrO₂ and CuAl_{0.5}Cr_{0.5}O₂ films prepared by sol-gel method. It was found that *p*-type conductivity and transmittance of the CuCrO₂ films were improved by Mg doping about two orders of magnitude and 16%, respectively. As a result, the CuCr_{0.9}Mg_{0.1}O₂ film with the transparency of about 47% and the resistivity of 1.13 Ω cm can be realized. Nevertheless, the films prepared by sol-gel method have the electrical stability even at high-temperature because the synthetic procedure has included the high-temperature annealing process. In addition, the sol-gel technique offers a high flexibility regarding material composition and the introduction of dopants due to its variability of stoichiometry. It is also a widely used industrial technique in numerous large scale production lines. However, most delafossite films have been prepared by vacuum based technologies, such as pulsed laser deposition and sputtering,^{20,21} owing to the instability of Cu⁺ and the sensibility of the oxygen partial pressure. Note that the preparation of Mg-doped CuCrO₂ film has been reported by some groups.^{11,17,21} Nevertheless, the intrinsic mechanisms of optical response behavior and electrical transport of Mg-doped CuCrO₂ films have been paid less attention. Recently, we have successfully synthesized the CuGaO₂ and CuGa_{1-x}Cr_xO₂ ($0 \leq x \leq 1$) films by sol-gel method.^{9,22} The microstructure, phonon modes, optical properties, and electronic band structures have been discussed. The CuGa_{0.8}Cr_{0.2}O₂ film was found to have the largest electrical conductivity of 0.071 S cm⁻¹ among the CuGa_{1-x}Cr_xO₂ films at room temperature. In order to further optimize the material/device performances, the growth and physical properties of the CuCr_{1-x}Mg_xO₂ system are worth studying due to the fact that the Mg-doping can significantly improve its electrical characteristic.

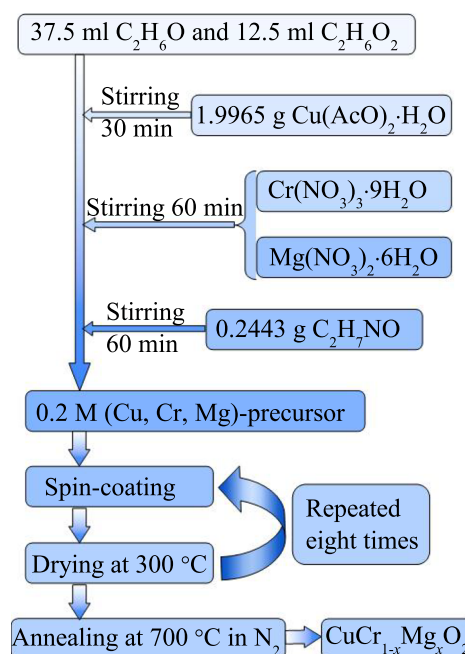
In this work, the CuCr_{1-x}Mg_xO₂ ($0 \leq x \leq 12\%$) films were prepared by the sol-gel method. It was found that Mg-doping affects the microstructure and improves the film crystal quality with the enhancement of the (00l) preferred orientation. The spectral transmittance of the films approach about 70%–75% in the visible-near-infrared region. Moreover, the highest electrical conductivity is estimated to about 3.85 S cm⁻¹ at room temperature for the CuCr_{0.88}Mg_{0.12}O₂ film, which is four-order magnitude larger than that of pure

CuCrO₂ film. The high transmittance and conductivity of films indicated that they can be used for the visible or near-infrared active devices.

II. EXPERIMENTAL DETAILS

A. Fabrication of CuCr_{1-x}Mg_xO₂ films

The CuCr_{1-x}Mg_xO₂ films were deposited on (001) sapphire substrates by the sol-gel route employing a spin-coating process. In order to obtain the effects of Mg compositions on optical and electrical properties, the films were fabricated in the Mg composition range of 0–12 mol. % with the interval of 2 mol. %, i.e., the mole compositions of Mg atoms were 0%, 2%, 4%, 6%, 8%, 10%, and 12%, respectively. Analytically pure chromium nitrate hydrate [Cr(NO₃)₃ · 9H₂O], magnesium nitrate hydrate [Mg(NO₃)₂ · 6H₂O], and copper(II) acetate hydrate [Cu(AcO)₂ · H₂O] were used as the starting materials. The copper(II) material was chosen due to the instability of Cu⁺ and the experimental condition. The sol was synthesized as shown in Scheme 1. First, anhydrous ethanol [C₂H₆O] and ethylene glycol [C₂H₆O₂] were mixed with a required volume ratio of 3:1 under magnetic stirring. In other words, the components of a 50 ml mixture solvent were 37.5 and 12.5 ml for anhydrous ethanol and ethylene glycol, respectively. Then, 1.9965 g copper acetate hydrate was dissolved in the mixture solvent with stirring about 30 min, yielding a blue transparent solution. After the solution was stable and homogeneous, the required chromium nitrate hydrate and magnesium nitrate hydrate were added into the solution. The mass was counted by the mole ration of [Mg²⁺]/[Cr³⁺]. Stirring was continuous until they were completely dissolved, yielding a dark blue solution. The 0.2443 g ethanolamine [C₂H₇NO, 99%] as additive was added, and the magnetic stirring at room temperature was carried out again for 1 h. Note that the [C₂H₇NO]/[Cu²⁺] molar ratio of solution was 1:2.5.



SCHEME 1. Process of the preparation for Mg-doped CuCrO₂ precursors and films.

Prior to the deposition, the sapphire substrates were cleaned through nitric acid, deionized water, acetone, and ethanol with ultrasonic cleaner sequentially. The transparent and homogeneous precursors were spin-coated onto (001) sapphire substrates at a speed of 4000 rpm for 20 s. The deposited films were preheated at 300 °C for 5 min in air to evaporate the solvent and remove organic residues in a rapid thermal processing. In order to obtain the films with desired thickness, the above process (spin-coating and preheating) was repeated eight times. Finally, the films were annealed at 700 °C for 30 min in N₂ with a flow of 2.5 l/min.

B. XRD, AFM, SEM, Raman, transmittance, and electrical measurements

The crystalline structure of CuCr_{1-x}Mg_xO₂ (0 ≤ x ≤ 12%) films was investigated by X-ray diffraction (XRD) using a Ni filtered Cu K α radiation source (D/MAX-2550 V, Rigaku Co.). In the XRD measurement, a vertical goniometer (Model RINT2000) was used, and continuous scanning mode (θ -2 θ) was selected with an interval of 0.02° and the scanning rate of 10°/min. The surface morphology was investigated by atomic force microscopy (AFM) with the contacting mode in areas of 2 × 2 μm^2 (Digital Instruments Dimension Icon, Bruker). The surface and cross-section microstructure of films were characterized using a scanning electron microscope (SEM, S-3000N, Philips XL30FEG). Raman scattering experiments were carried out by a micro-Raman spectrometer (Jobin-Yvon LabRAM HR 800 UV) with a 488 nm Ar⁺ laser. The transmittance spectra were recorded by a double beam ultraviolet-infrared spectrophotometer (Perkin Elmer UV/VIS Lambda 950) at the wavelength region of 2650–190 nm (0.5–6.5 eV) with the interval of 2 nm at room temperature. Due to the high resistance values and the larger change of resistance with the temperature, it is impossible to perform four point method for variable temperature measurement. Thus, two point method was applied in the present work. First, the electrodes of Pt were sputtered on both ends of the well-defined rectangle samples for Ohmic contact. Then, the outgoing wire of electrodes was fixed with silver paste after a drying step. The samples were mounted into a Linkam THMSE 600 heating stage for variable temperature experiments from 80 to 400 K. The temperature can be controlled within the accuracy of 0.1 K. The possible oxidation of the film during the heating and cooling process can be avoided under nitrogen atmosphere. A Keithley 6430 source meter was applied to provide an external direct-current voltage to the sample via Pt electrodes, and the resistance value can be recorded. In addition, Hall measurements were made by Van der Pauw method at room temperature and the positive hall coefficients confirm *p*-type behavior of CuCr_{1-x}Mg_xO₂ films.

III. RESULTS AND DISCUSSION

A. Structural and morphology characterizations

The X-ray diffraction θ -2 θ scans of CuCr_{1-x}Mg_xO₂ films with different Mg compositions of 0–12 mol. % deposited on (001) sapphire substrates are shown in Fig. 1. It can be seen that all films are polycrystalline with a stronger

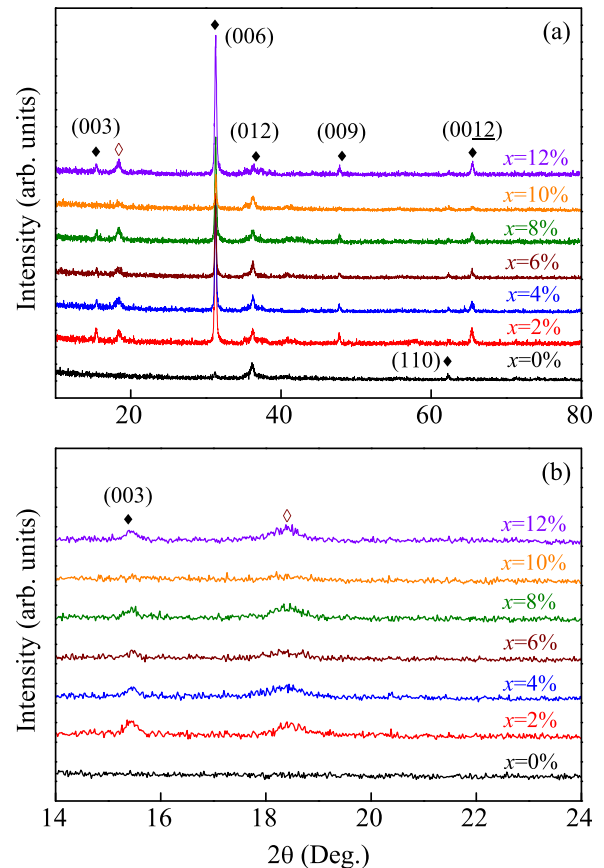


FIG. 1. (a) XRD patterns of the CuCr_{1-x}Mg_xO₂ (0 ≤ x ≤ 12%) films grown on (001) sapphire substrates with 2 θ = 10° to 80°. (b) An enlarging region of 2 θ = 14° to 24° to obviously show the minority phase peak. Note that the symbol (◆) indicates the delafossite phase, while the peak indicated by the symbol (◊) corresponds to the cubic spinel phase.

(006) diffraction peak, except that the (012) diffraction peak is the strongest for the CuCrO₂ film. It indicates that the films with Mg-doping are preferentially oriented along the *c*-axis perpendicular to the substrate surface and the Mg-doping induces the appearance of the cubic spinel phase (the peak at 18.6°). Both the copper and magnesium components can act as divalent A-site ions in the spinel crystal AB₂O₄ lattice (CuCr₂O₄ JCPDF Card No. 26-0509 and MgCr₂O₄ JCPDF Card No. 10-0351). They almost exhibit identical diffraction pattern, so it is impossible to distinguish these two spinel phases or even mixed forms by X-ray diffraction.¹¹ Generally, the spinel phase should increase with increasing Mg composition. Sadik *et al.* reported that the relative intensities of the spinel peaks increase with an increment of Mg-composition for CuCr_{1-x}Mg_xO₂ (0 ≤ x ≤ 5%) films grown by pulsed laser deposition.²³

During the film preparation processing, a two-step annealing was used for the fabrication.¹⁰ In the first processing (the rapid thermal processing at 300 °C in air), the solvent and organic residues were removed and the amorphous spinel-type CuCr₂O₄ was formed. In the second processing of N₂ atmosphere, the spinel phase is converted with residual CuO to form the delafossite phase according to the following reaction: CuCr₂O₄ + CuO → 2CuCrO₂ + 1/2O₂. For spinel phase CuCr₂O₄, the samples exhibit a more amorphous character with increasing Mg composition, which is in favor of

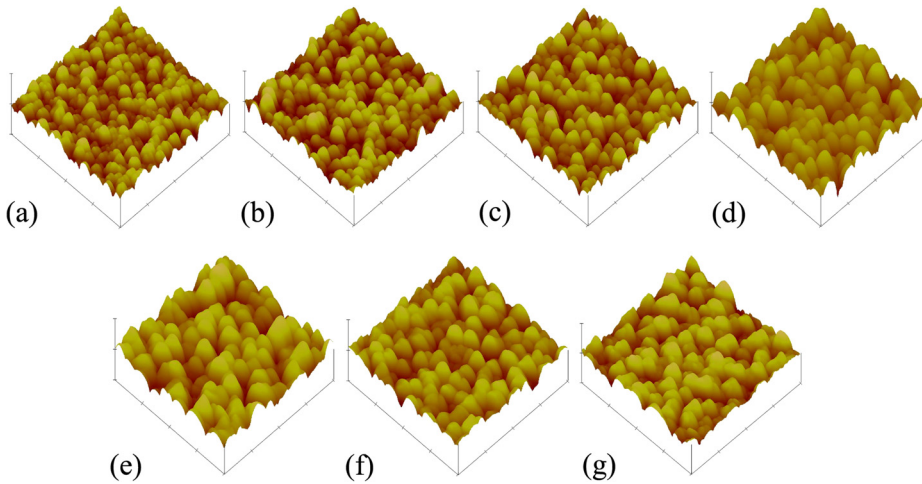


FIG. 2. AFM three-dimensional images of the CuCr_{1-x}Mg_xO₂ films with the Mg compositions of (a) 0%, (b) 2%, (c) 4%, (d) 6%, (e) 8%, (f) 10%, and (g) 12%, respectively. Note that the scale height is 80 nm and the measured area is $2 \times 2 \mu\text{m}^2$.

the delafossite fabrication.¹¹ Thus, the crystal quality of films was improved by Mg-doping, as shown in Fig. 1(a). There is a change of Cu(II) to Cu(I) during the film fabrication processing by sol-gel method. The appearance of the cubic spinel phase is difficult to avoid because the phase transition is essential for the formation of the delafossite. Nevertheless, the cubic spinel phase is tiny and its effect is weaker as compared with the delafossite phase. It can be confirmed by the fact that the film conductivity is surprisingly increased by Mg doping (the detail discussion can be seen in the electrical transport part). In addition, XRD patterns are given in an enlarged scale for easily surveying the spinel phase, which is shown in Fig. 1(b). However, the change of the spinel peak cannot be derived intuitively. The spinel phases of CuCr₂O₄ and MgCrO₂ were not distinguished by X-ray diffraction, which suggests that the amount of impurities cannot be obtained. In order to compensate the deficiency of XRD, the Raman measurement was used and the results are shown in Fig. 4.

The AFM three-dimensional images of CuCr_{1-x}Mg_xO₂ films are shown in Fig. 2 and the film grains are closely gathered and densely arranged. The root-mean-square roughness of surface is 7.89, 8.81, 9.94, 14.6, 23.9, 16.5, and 17.8 nm for $x = 0\%$, 2%, 4%, 6%, 8%, 10%, and 12%, respectively. It can be seen that the root-mean-square roughness increased first, and decreased with increasing Mg-composition. The grain size change also shows the similar variation trend,

which is due to the two effects induced by Mg-doping: (a) the crystal quality was increased by Mg-doping, which induced the increase of grain size; (b) the doping resulted in more crystal defects and grain boundaries, which inhibit the growth of grain. For $x \leq 8\%$, the former effect is larger than latter one because the roughness is increased with increment of Mg-composition. However, the case is just on the contrary for a higher doping. The AFM measurement is a surface characterization, which is related to the test zone. For comprehensive and visual studies, the SEM measurement was used in the present work. The surface and cross-sectional SEM images of CuCr_{1-x}Mg_xO₂ ($0 \leq x \leq 12\%$) films are shown in Fig. 3. The grain size increased first, and decreased with increasing Mg-composition. Moreover, the surface pattern also varied with the change of Mg-composition. For CuCrO₂ film, the grain size is homogeneous and often has hexagonal shaped crystallites, which can be identified as the delafossite.¹¹ Whereas the smaller spherical particles probably represent the spinel phase induced by Mg-doping, as shown in Figs. 3(b)–3(g). When the Mg-composition is beyond 6%, the surface ablating increases and the grain boundary becomes concealed. From the cross-sectional image (h), the thickness of the CuCr_{0.96}Mg_{0.04}O₂ film is about 320 nm. Therefore, the root-mean-square roughness (9.94 nm) is approximately 3.1% of its thickness. The sample is composed of particles, which does not show the visible layer boundary.

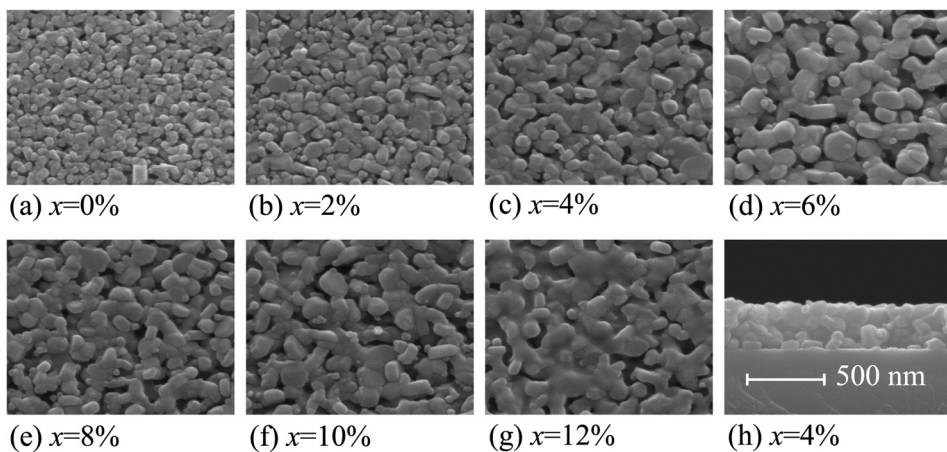


FIG. 3. The surface SEM images of the CuCr_{1-x}Mg_xO₂ ($0 \leq x \leq 12\%$) films, whose magnification ratio is 1:40 000. Note that the picture (h) indicates the cross-sectional image for the film with the Mg composition of 4%, and the scale is given in this picture.

B. Raman scattering

Fig. 4 shows Raman spectra of $\text{CuCr}_{1-x}\text{Mg}_x\text{O}_2$ ($0 \leq x \leq 12\%$) films recorded at room temperature. Generally, the delafossite compound is characterized by rhombohedral symmetry with the point group $3m$ (C_{3v}) and the space group $R\bar{3}m$ (C_{3v}^6), with four atoms in the primitive cell, which gives rise to 12 normal modes.²⁴ According to the group theory, a general mode at the Brillouin zone center as $\Gamma = A_{1g} + E_g + 3A_{2u} + 3E_u$, out of which A_{1g} and E_g symmetry are Raman active modes.²⁵ The A mode implies the atomic vibration in the direction of Cu-O bond along the hexagonal c -axis. However, double degenerate E mode describes movement in the perpendicular direction, in which the odd modes denoted with the u subscript are infrared active and acoustic modes. Interestingly, the infrared-active mode of E_u peak is observed, which is from the structural distortions. For $x=0\%$, Raman scattering peaks were observed around 101 cm^{-1} (E_u), 210 cm^{-1} (A_g), 456 cm^{-1} (E_g), and 709 cm^{-1} (A_{1g}), respectively. It agrees well with previous experimental results and the report of Amami *et al.*^{22,26} For $x=12\%$, Raman scattering peaks were observed around 99 cm^{-1} (E_u), 208 cm^{-1} (A_g), 456 cm^{-1} (E_g), and 709 cm^{-1} (A_{1g}), respectively. The change of peaks is actually tiny, which indicates that the delafossite structure was not severely broken by Mg-doping. On the other hand, the increase of the crystal quality by Mg-doping may neutralize some part of its structure break. For the films with Mg-composition beyond 6%, Raman active phonon modes of the cubic spinel phase are found and marked by symbol (\diamond) in Fig. 4. It is because Mg-doping induces the appearance of the cubic spinel phase, as previously discussed.

C. Optical properties

The transmittance spectra of $\text{CuCr}_{1-x}\text{Mg}_x\text{O}_2$ ($0 \leq x \leq 12\%$) films were measured in the wavelength range of $190\text{--}2650\text{ nm}$, as shown in Fig. 5. Although the $\text{CuCr}_{1-x}\text{Mg}_x\text{O}_2$ films are colored by Cr^{3+} ions, they have an optical transmittance of $70\%\text{--}75\%$ in the visible range. The energy level of Cr ions

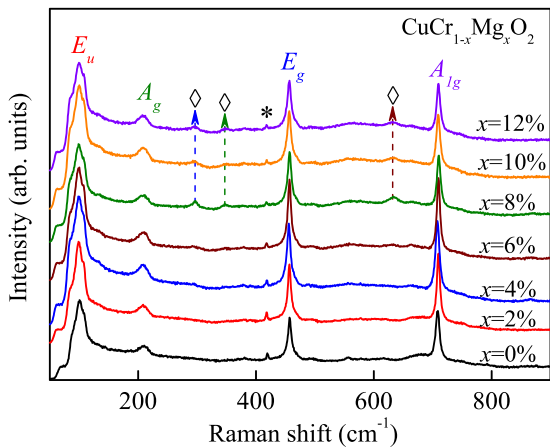


FIG. 4. Raman spectra of the $\text{CuCr}_{1-x}\text{Mg}_x\text{O}_2$ ($0 \leq x \leq 12\%$) films under the excitation line of 488 nm . Note that the dashed lines show the positions of Raman-active phonon modes from the cubic spinel phase, indicated by the symbol (\diamond). In addition, the symbol (*) indicates the observed trace from the sapphire substrate.

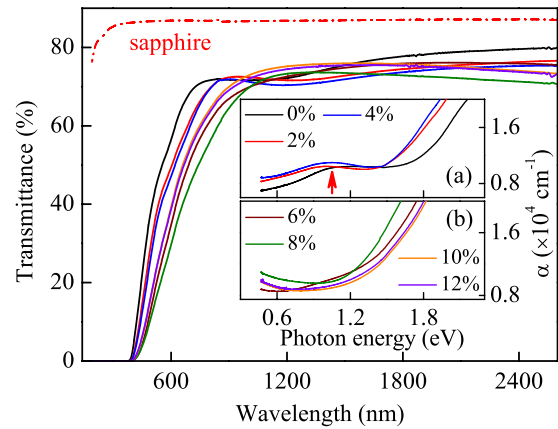


FIG. 5. Transmittance spectra of the $\text{CuCr}_{1-x}\text{Mg}_x\text{O}_2$ ($0 \leq x \leq 12\%$) films. For comparison, the dashed line is the transmittance spectrum of the sapphire substrate. The inset (a) shows the absorption coefficient for the films with the Mg composition below 6%; and the inset (b) shows the absorption coefficient for the films with a higher Mg composition. Note that the arrow in the inset (a) indicates that there is a minimal band gap for the $\text{CuCr}_{1-x}\text{Mg}_x\text{O}_2$ films.

from partially filled 3d shell will split into several levels according to the ligand field theory. The excitation of electrons from the lower to the upper of these levels could happen by absorbing photons in the visible range, which further induces the coloration for films with a higher Cr composition.^{10,17} The transmittance is larger than the result of 47% for $\text{CuCr}_{0.9}\text{Mg}_{0.1}\text{O}_2$ films reported by Bywalez *et al.*¹¹ and is close to the result of CuAlO_2 film prepared by the polymer-assisted deposition technique.²⁷ Moreover, the transmittance for near-infrared range approaches 75%. The high transmittance indicates that they can be used in the visible or the near-infrared active devices. For films with Mg-composition below 8%, the absorption edge presents a redshift trend with increment of Mg-doping. However, for Mg-composition beyond 8%, the absorption edge shows a blueshift variation, which also can be observed from the absorption coefficient in the insets. The inset (a) in Fig. 5 shows the absorption coefficient of $\text{CuCr}_{1-x}\text{Mg}_x\text{O}_2$ films with Mg-composition below 6%. The minimal energy level about $1.03\text{--}0.95\text{ eV}$ can be easily seen for the $\text{CuCr}_{1-x}\text{Mg}_x\text{O}_2$ films. It has a little redshift with increasing x , and disappears for films with Mg-composition beyond 6%, as shown in Fig. 5(b). In addition, the undoped CuCrO_2 film shows an abrupt absorbance change in the band gap energy region, as compared to a gradual change for Mg-doped films. It indicates that the impurity energy levels and the tail states were induced by Mg-doping.

Fig. 6 shows the optical band gap energies of $\text{CuCr}_{1-x}\text{Mg}_x\text{O}_2$ ($0 \leq x \leq 12\%$) films. The optical band gap (E_{OBG}) is deduced by Tauc's relation $(\alpha h\nu)^n = C(h\nu - E_{\text{OBG}})$, α denotes the absorption coefficient which is obtained by the relation, $\alpha = -\ln(T)/d$, where d is the film thickness and T is the transmittance of film.²⁸ The nature of band gap is identified by the exponent n , and an intercept of $(\alpha h\nu)^n$ plot with the photon energy $h\nu$ yields the optical band gap energy. Fig. 6 displays the $(\alpha h\nu)^n$ versus $h\nu$ plots, with $n=2$ for direct band gap ($E_{\text{OBG}}^{\text{dir}}$) and $n=1/2$ for indirect band gap ($E_{\text{OBG}}^{\text{indir}}$) transitions of $\text{CuCr}_{1-x}\text{Mg}_x\text{O}_2$ films. In Fig. 6(a), the direct optical band gaps for $\text{CuCr}_{1-x}\text{Mg}_x\text{O}_2$

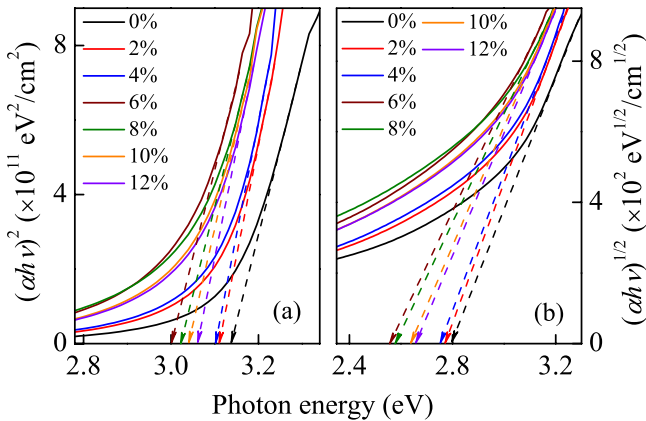


FIG. 6. (a) Plots of $(\alpha h\nu)^2$ vs the photon energy for the estimation of direct optical band gap energies from the $\text{CuCr}_{1-x}\text{Mg}_x\text{O}_2$ ($0 \leq x \leq 12\%$) films. (b) Plots of $(\alpha h\nu)^{1/2}$ vs the photon energy for the estimation of indirect band gap energies from the $\text{CuCr}_{1-x}\text{Mg}_x\text{O}_2$ ($0 \leq x \leq 12\%$) films.

films are 3.14, 3.11, 3.10, 3.0, 3.02, 3.04, and 3.06 eV for $x = 0\%$, 2%, 4%, 6%, 8%, 10%, and 12%, respectively. In Fig. 6(b), the indirect band gaps are 2.79, 2.77, 2.75, 2.56, 2.58, 2.64, and 2.66 eV for $x = 0\%$, 2%, 4%, 6%, 8%, 10%, and 12%, respectively. Lim *et al.* also reported the fact that it has an indirect band gap at 2.58 eV, and a direct gap at 3.11 eV for $\text{CuCr}_{0.93}\text{Mg}_{0.07}\text{O}_2$ film prepared by the chemical spray pyrolysis deposition.²¹ Note that the transition of dominative absorption region from an indirect to a direct band occurs gradually without an inflection points. It indicates that the optical transitions should take place from the near points in valence band maximum in both direct and indirect cases.²⁹ Moreover, both direct and indirect band gaps decline and then climb up, which is due to the combined actions of band gap renormalization and Burstein-Moss effect induced by Mg-doping. For $\text{CuCr}_{1-x}\text{Mg}_x\text{O}_2$ films, Mg-doping induced the increment of carrier concentration, which strengthens the exchange and interaction of carriers. Then, the tail states and the band gap renormalization effect can be formed. The variation of band gap can be fitted by an equation: $\Delta E = \Delta E(0) - kp^{1/3}$, where p is the carrier concentration. There is a linear relation between the cube root of carrier concentration and the band gap. The factor k is estimated to about $3.12 \times 10^{-8} \text{ eV}/\text{cm}^3$.

Fig. 7 shows schematic representation for the electronic band structure of $\text{CuCr}_{1-x}\text{Mg}_x\text{O}_2$ films. The conduction band of films splits into energy levels, denoted by E_1 and E_2 , which are corresponding to electronic transitions indicated by ΔE_1 and ΔE_2 , respectively. The similar band gaps were reported in CuFeO_2 material within GGA (generalized-gradient approximations) calculations,³⁰ and first-principles calculations point toward the existence of indirect fundamental band gap for delafossite materials, which forms a tail of weak absorption below the optical band gap.³¹ Based on the theoretical results, Nie *et al.*³¹ and Vidal *et al.*³² both showed that the fundamental indirect gap in CuMO_2 ($M = \text{Al}, \text{Ga}, \text{In}$) occurs at the conduction band minimum at Γ point and valence band maximum near F point on the Γ - F line. Scanlon *et al.*³³ proved that the band structure of CuCrO_2 exhibits an indirect band gap of 2.04 eV, while the direct gap

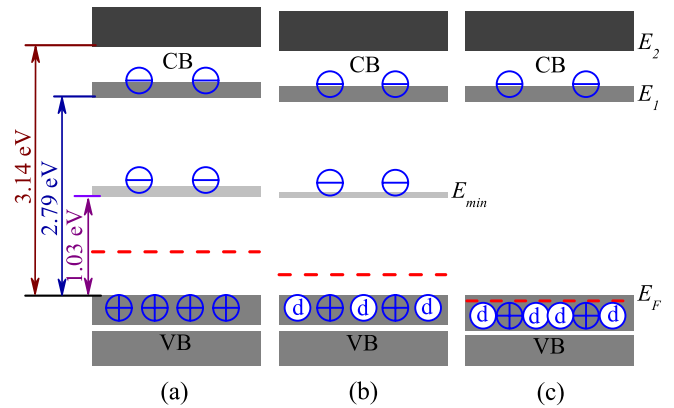


FIG. 7. Schematic representation of the electronic band structure for the $\text{CuCr}_{1-x}\text{Mg}_x\text{O}_2$ films with the Mg compositions of (a) 0%, (b) 6%, and (c) 12%, respectively. E_F denotes the Fermi energy level, E_{min} denotes the weak absorption energy level, E_1 and E_2 indicate the splitting energy levels of the conduction band. Note that the symbols (\oplus) and (\ominus) indicate the nature hole and electron of the CuCrO_2 material. However, the symbol (\odot) indicates the hole induced by Mg-doping.

is 2.55 eV and is found near M along M- Γ , which were studied by GGA+U (the density-functional theory with on-site corrections for strongly correlated systems). However, Robertson *et al.* predicted the valence-band maximum to be at L point, which was studied with the hybrid functional screened-exchange local density approximation (sX-LDA).^{34,35} They also reported that the indirect band gap opens to 2.9 eV between the F and L points and the minimum direct band gap is 3.1 eV at the L point. In addition, another direct band gap of 3.25 eV occurs at the F point. These above results agree well with the experimental values. Based on the theoretical work, ΔE_1 can be considered as the electronic transition between the valence-band maximum and the bottom of conduction band, which is the indirect transition. Correspondingly, ΔE_2 indicates the direct electronic transition. Note that the optical band gaps shown in Fig. 6 are the comprehensive performance of electronic transitions. In addition, the parameter E_{min} indicates the weak absorption energy level, as shown in Fig. 5. Even though the indirect gap has been reported as low as 1.28 eV or 1.45 eV,^{36,37} the E_{min} should be the defect states of some sort because such low energies are inconsistent with the theoretical results. Shin *et al.* pointed that the low energy absorption was associated with Cu^{2+} defect states arising from cation deficiency.³⁸ They also discussed the states of Cr^{3+} and excitations of those two states, which were found to be as larger than 2 eV. The theoretical work also suggests that cation vacancies are likely to be the dominant native defect in copper delafossite materials.³⁹

The detailed variation of band gaps with Mg-composition is discussed as follow. For the films with Mg-composition below 6%, the increment of Mg-composition would induce the increase of hole carrier, which will result in the form of tail states in the bottom of conduction band. Therefore, the optical band gap shows a redshift with the increment of Mg-composition. When the Mg-composition is beyond 6%, the highly doping induced the Fermi energy level going into the valence band, and formed the Burstein-Moss effect.⁴⁰ As

shown in Fig. 7(c), the optical band gap shows blueshift with the Mg composition. Thus, the $\text{CuCr}_{0.94}\text{Mg}_{0.06}\text{O}_2$ film has the smallest direct and indirect band gaps (3.0 and 2.56 eV) induced by the band gap renormalization and Burstein-Moss effect. Moreover, the minimal band energy faded away with the increment of Mg-composition. It is because that the hole carrier increment results in the electron hopping easily from the minimal energy level to the valence-band maximum. Therefore, the minimal energy level becomes weaker and finally disappears with increasing doping composition.

D. Electrical transport

To further understand the intrinsic characteristics of $\text{CuCr}_{1-x}\text{Mg}_x\text{O}_2$ films, the temperature dependence of electrical conductivity should be discussed, as shown in Fig. 8. Note that the temperature ranges in Figs. 8(a) and 8(b) are 150–400 K and 80–220 K, respectively. They indicate different behaviors of the electrical transport for $\text{CuCr}_{1-x}\text{Mg}_x\text{O}_2$ films. As can be seen in Fig. 8(a), the $\text{CuCr}_{1-x}\text{Mg}_x\text{O}_2$ films show a thermal activation behavior at high temperature because the plots of $\ln\sigma$ vs. $1000/T$ show a linear change.^{8,20} In higher temperature region, the hopping of holes between nearest-neighbor Cu sites determines the electrical transport properties.⁴¹ The slope coefficient k determined by the linear fit of each curve is shown in Fig. 9(a). The conductivity of films at higher temperature can be expressed by $\sigma = A\exp(-E_a/k_B T)$, where E_a is the thermal activation energy, k_B is Boltzmann constant, and A is a constant. The estimated E_a values are 292, 187, 87, 70, 55, 47, and 42 meV for $x=0\%$, 2%, 4%, 6%, 8%, 10%, and 12%, respectively, as shown in Fig. 9(b). The evaluated activation energy is much smaller than half of the band gap, which indicates that the hole transport in the valence band is thermally activated from an acceptor. A continuous decrease in E_a values with increasing Mg-doping was clearly observed. The change should be due to the variation of Fermi level for $\text{CuCr}_{1-x}\text{Mg}_x\text{O}_2$ films. The Mg-doping induced the Fermi level moving to the top of

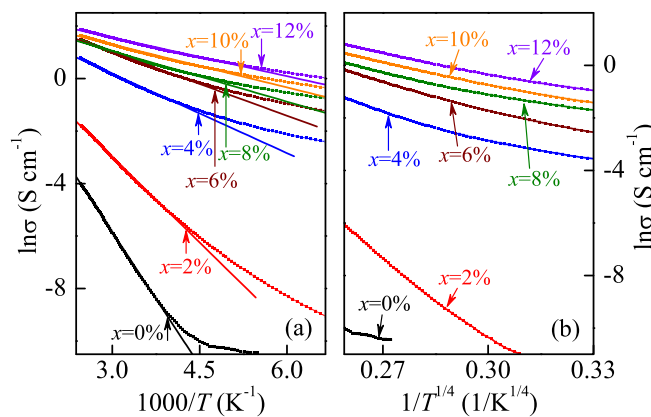


FIG. 8. (a) Plots of $\ln\sigma$ vs $1000/T$ of the $\text{CuCr}_{1-x}\text{Mg}_x\text{O}_2$ ($0 \leq x \leq 12\%$) films, and the linear fit of each curve determines the slope coefficient k . The arrows show the sample labels with the different component of Mg-doping. The positions of the arrows indicate the crossover (T_{cross}) at which the electric conductivity starts to deviate from the thermal activation behavior. Note that the temperature range is 150–400 K. (b) Plots of $\ln\sigma$ vs $1/T^{1/4}$ of the $\text{CuCr}_{1-x}\text{Mg}_x\text{O}_2$ ($0 \leq x \leq 12\%$) films, and the temperature range is 80–220 K.

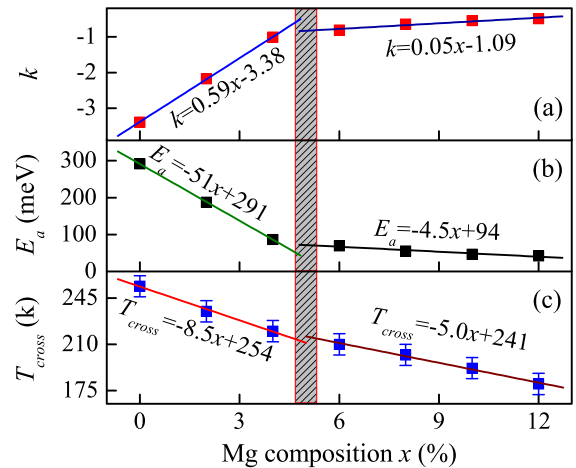


FIG. 9. The Mg composition dependence of (a) the slope coefficient k , (b) the activation energy E_a , and (c) T_{cross} at which the electric conductivity deviates from a thermal activation behavior, respectively. The solid lines and equations represent the linear fitting results to guide the eyes. Note that the shade part indicates different composition dependence behavior.

valence band, and the carriers can easily jump to the Fermi level from valence band.⁴² In addition, it should be noted that the variation rates are different for two ranges of $0 \leq x < 6\%$ and $6 \leq x \leq 12\%$, respectively. As can be seen from the fitted equations, the variation rate of $\text{CuCr}_{1-x}\text{Mg}_x\text{O}_2$ films with Mg-composition below 6% is ten times larger than that of other films. It shows that most of Mg ions can substitute for Cr ions forming the doped holes. However, with increasing Mg-composition, the effective substitute behavior becomes weaker and most of over-doping Mg ions may not occupy the nature structure. They may be the spinel phase of MgCr_2O_4 or the amorphous state of MgO , which can disperse in films. Note that the arrows in Fig. 8(a) show not only the sample labels with different component of Mg-doping but also the positions indicating the crossover (T_{cross}) temperature, at which the electric conductivity presents the change from the thermal activation behavior to that of three-dimensional variable range hopping.

Plots of $\ln\sigma$ vs. $1/T^{1/4}$ for $\text{CuCr}_{1-x}\text{Mg}_x\text{O}_2$ ($0 \leq x \leq 12\%$) films can be seen in Fig. 8(b), whose linear characteristic indicates the behavior of three-dimensional variable range hopping at lower temperature (below T_{cross}). The crossover was previously observed in other delafossite films, such as CuAlO_2 ,⁸ CuGaO_2 ,²⁰ and AgGaO_2 .⁴³ In lower temperature region, the thermal energy weakening may depress the hole hopping between the nearest-neighbor Cu sites, and the contribution of Cr site hopping becomes more dominant. Hence, the hopping to the Cu site in other Cu layers becomes relatively dominant. The conductivity shows the three-dimensional variable range-hopping behavior.⁴¹ The detailed crossover values are shown in Fig. 9(c). Obviously, the T_{cross} temperature decreases with increasing Mg-composition, which is due to the change of spin-charge coupling between the doped hole and the local spin at Cr site. In other words, for $\text{CuCr}_{1-x}\text{Mg}_x\text{O}_2$ films, the spin fluctuation of local spin at Cr sites is disturbed at a lower temperature due to the substitution at Cr^{3+} site of the Mg^{2+} ion. Therefore, the influence of doped holes increases with Mg-composition.

The results derived from the Hall effect measurement for $\text{CuCr}_{1-x}\text{Mg}_x\text{O}_2$ films are listed in Table I. The positive Hall coefficient demonstrates the *p*-type conduction behavior. The substitution at Cr^{3+} site of the Mg^{2+} ion induces the hole and the concentration of hole carrier is increased with Mg-doping composition. By contrast, the Hall mobility decreases with the increment of Mg-composition, especially for the films with the composition above 6%. The result can be attributed to the effect of the ionized impurity scattering. The increasing dopant concentration might lead to the shift of Fermi level from the conduction band minimum towards the valence band maximum and facilitate the formation of donor-like defects.^{44,45} For films with Mg-doping, holes may be introduced into the upper part of the valence band by oxidation of Cu^+ formally found in stoichiometric CuCrO_2 to the Cu^{2+} state, which also may be achieved either by cation deficiency or incorporation of oxygen interstitial.⁴⁶ Thus, the spinel phase CuCr_2O_4 was formed with Mg-doping, as shown in XRD patterns. In addition, a dopant Mg^{2+} ion will act as donor rather than an acceptor if it occupies a Cu^+ site rather than a Cr^{3+} site,⁴⁷ which induced the compensation of the intended acceptor doping. Therefore, the conductivity increment becomes small for Mg-composition above 6%. As shown in Table I, the effective carrier concentration can be derived by Hall measurement. It is easy to see that the variation of the carrier concentration with Mg-composition below 6% is obviously larger than that of the films with a higher Mg composition.

It is worth to be noted that the highest conductivity of 3.85 S cm^{-1} corresponds to the largest magnesium dopant level of up to 12%, which is four orders of magnitude larger than that of the pure CuCrO_2 film with $8.81 \times 10^{-4} \text{ S cm}^{-1}$. It indicates that the doping by bivalence ions is an effective way to improve the electrical property of delafossite material. The result is better than that of $7.34 \Omega \text{cm}$ for $\text{CuCr}_{0.95}\text{Mg}_{0.05}\text{O}_2$ film prepared by Wang *et al.*⁴⁸ and the best conductivity among $\text{CuCr}_{1-x}\text{Mg}_x\text{O}_2$ ($0 \leq x \leq 15\%$) films reported by Bywalez *et al.*¹¹ Although there are other reports on the fact that the doping of divalent element (e.g., Mg, Ca) greatly increases the electrical conductivity of other delafossite compounds,^{49,50} the Mg-doped CuCrO_2 material is enjoyed in the future due to its good thermal stability and well electrical properties. In addition, the $\text{CuCr}_{1-x}\text{Mg}_x\text{O}_2$ films prepared by sol-gel technique owned a high flexibility of composition and a low synthesis temperature, which make

TABLE I. The electrical properties of the $\text{CuCr}_{1-x}\text{Mg}_x\text{O}_2$ ($0\% \leq x \leq 12\%$) films at room temperature.

Mg composition (mol. %)	Conductivity (S cm^{-1})	Hall coefficient ($\text{cm}^3 \text{C}^{-1}$)	Hall mobility ($\text{cm}^2 \text{V}^{-1} \text{s}^{-1}$)	Carrier concentration (cm^{-3})
0	8.81×10^{-4}	4.41×10^3	3.89	1.42×10^{15}
2	2.37×10^{-2}	4.60×10^1	1.09	1.36×10^{17}
4	8.32×10^{-1}	2.96×10^{-1}	0.25	2.11×10^{19}
6	2.03	1.90×10^{-1}	0.39	3.29×10^{19}
8	2.21	1.53×10^{-2}	0.03	4.07×10^{20}
10	2.94	7.15×10^{-3}	0.02	8.73×10^{20}
12	3.85	7.21×10^{-3}	0.03	8.66×10^{20}

it possible to be widely used in industrial production. Especially, the transmittance approaches 70%–75% in the visible region and the highest electrical conductivity is 3.85 S cm^{-1} at room temperature for $\text{CuCr}_{1-x}\text{Mg}_x\text{O}_2$ films. The high transmittance and larger conductivity will make *p*-type $\text{CuCr}_{1-x}\text{Mg}_x\text{O}_2$ films promising for applications in the optoelectronic devices.

IV. CONCLUSION

In summary, we prepared *p*-type $\text{CuCr}_{1-x}\text{Mg}_x\text{O}_2$ ($0 \leq x \leq 12\%$) films on (001) sapphire substrates by sol-gel method. It was found that the Mg-doping induced the change of film microstructure. It improved the crystal quality with the enhancement of the (001) preferred orientation. For films with Mg-composition beyond 6%, the cubic spinel phase phonon modes are found in Raman spectra. The spectral transmittance of films approaches about 70%–75% in the visible region. The direct and indirect band gap decline and then climb up with increasing Mg-doping composition. When x equals 6%, there are the smallest band gap values of 3.0 and 2.56 eV, respectively. For films with Mg-composition below 6%, the redshift of optical band gap is due to the effect of tail states and band gap renormalization effect. When the Mg-composition is beyond 6%, the band gap blueshift is caused by Burstein-Moss effect. In addition, the temperature dependence on electrical conductivity was studied for $\text{CuCr}_{1-x}\text{Mg}_x\text{O}_2$ films. In higher temperature region, the hopping of holes between the nearest-neighbor Cu sites may determine the electrical transport properties. However, for lower temperature region, the hopping to the Cu site in other Cu layers becomes relatively dominant so that the conductivity shows the three-dimensional variable range-hopping behavior. The increasing Mg-doping composition induces the crossover temperature values from 254 to 180 K. The highest electrical conductivity is estimated to be about 3.85 S cm^{-1} at room temperature for $x=12\%$. The low synthesis temperature and high electrical conductivity will make the Mg-doped CuCrO_2 material wide-applications in the future.

ACKNOWLEDGMENTS

One of the authors (M. J. Han) is grateful to Qian Yu and Xia Zhu for the technical supports. This work was financially supported by Major State Basic Research Development Program of China (Grant Nos. 2011CB922200 and 2013CB922300), Natural Science Foundation of China (Grant Nos. 11374097, 61376129, 11074076, and 61106122), Projects of Science and Technology Commission of Shanghai Municipality (Grant Nos. 13JC1402100, 13JC1404200, and 11520701300), and the Program for Professor of Special Appointment (Eastern Scholar) at Shanghai Institutions of Higher Learning.

¹Y. Z. Zheng, X. Tao, L. X. Wang, H. Xu, Q. Hou, W. L. Zhou, and J. F. Chen, *Chem. Mater.* **22**, 928 (2010).

²C. G. Granqvist, *Sol. Energy Mater. Sol. Cells* **91**, 1529 (2007).

³T. Minami, *Semicond. Sci. Technol.* **20**, S35 (2005).

⁴A. J. Chiquito, A. J. C. Lanfredi, R. F. M. de Oliveira, L. P. Pozzi, and E. R. Leite, *Nano Lett.* **7**, 1439 (2007).

- ⁵Y. M. Kim, W. J. Lee, D.-R. Jung, J. M. Kim, S. H. Nam, H. C. Kim, and B. W. Park, *Appl. Phys. Lett.* **96**, 171902 (2010).
- ⁶F. Yang and S. R. Forrest, *Adv. Mater.* **18**, 2018 (2006).
- ⁷R. S. Ajimsha, K. A. Vanaja, M. K. Jayaraj, P. Misra, V. K. Dixit, and L. M. Kukreja, *Thin Solid Films* **515**, 7352 (2007).
- ⁸H. Kawazoe, M. Yasukawa, H. Hyodo, M. Kurita, H. Yanagi, and H. Hosono, *Nature* **389**, 939 (1997).
- ⁹M. J. Han, K. Jiang, J. Z. Zhang, Y. W. Li, Z. G. Hu, and J. H. Chu, *Appl. Phys. Lett.* **99**, 131104 (2011).
- ¹⁰S. Götzendörfer, C. Polenzky, S. Ulrich, and P. Löbmann, *Thin Solid Films* **518**, 1153 (2009).
- ¹¹R. Bywalez, S. Götzendörfer, and P. Löbmann, *J. Mater. Chem.* **20**, 6562 (2010).
- ¹²M. Lalanne, A. Barnabé, F. Mathieu, and Ph. Tailhades, *Inorg. Chem.* **48**, 6065 (2009).
- ¹³D. O. Scanlon, K. G. Godinho, B. J. Morgan, and G. W. Watson, *J. Chem. Phys.* **132**, 024707 (2010).
- ¹⁴N. Duan, A. W. Sleight, M. K. Jayaraj, and J. Tate, *Appl. Phys. Lett.* **77**, 1325 (2000).
- ¹⁵R. D. Shannon, *Acta Crystallogr. A* **32**, 751 (1976).
- ¹⁶D. Li, X. D. Fang, Z. H. Deng, S. Zhou, R. H. Tao, W. W. Dong, T. Wang, Y. P. Zhao, G. Meng, and X. B. Zhu, *J. Phys. D: Appl. Phys.* **40**, 4910 (2007).
- ¹⁷R. Nagarajan, A. D. Draeseke, A. W. Sleight, and J. Tate, *J. Appl. Phys.* **89**, 8022 (2001).
- ¹⁸M. A. Marquardt, N. A. Ashmore, and D. P. Cann, *Thin Solid Films* **496**, 146 (2006).
- ¹⁹H. Yanagi, T. Hase, S. Ibuki, K. Ueda, and H. Hosono, *Appl. Phys. Lett.* **78**, 1583 (2001).
- ²⁰K. Ueda, T. Hase, H. Yanagi, H. Kawazoe, H. Hosono, H. Ohta, M. Orita, and M. Hirano, *J. Appl. Phys.* **89**, 1790 (2001).
- ²¹S. H. Lim, S. Desu, and A. C. Rastogi, *J. Phys. Chem. Solids* **69**, 2047 (2008).
- ²²M. J. Han, K. Jiang, J. Z. Zhang, W. L. Yu, Y. W. Li, Z. G. Hu, and J. H. Chu, *J. Mater. Chem.* **22**, 18463 (2012).
- ²³P. W. Sadik, M. Ivill, V. Craciun, and D. P. Norton, *Thin Solid Films* **517**, 3211 (2009).
- ²⁴J. Pellicer-Porres, A. Segura, E. Martínez, A. M. Saitta, A. Polian, J. C. Chervin, and B. Canny, *Phys. Rev. B* **72**, 064301 (2005).
- ²⁵S. P. Pavunny, A. Kumar, and R. S. Katiyar, *J. Appl. Phys.* **107**, 013522 (2010).
- ²⁶M. Amami, C. V. Colin, P. Strobel, and A. Ben Salah, *Physica B* **406**, 2182 (2011).
- ²⁷H. M. Luo, M. K. Jain, T. M. McCleskey, E. Bauer, A. K. Burrell, and Q. X. Jia, *Adv. Mater.* **19**, 3604 (2007).
- ²⁸H. Hiramatsu, W.-S. Seo, and K. Koumoto, *Chem. Mater.* **10**, 3033 (1998).
- ²⁹A. C. Rastogi, S. H. Lim, and S. B. Desu, *J. Appl. Phys.* **104**, 023712 (2008).
- ³⁰K. P. Ong, K. W. Bai, P. Blaha, and P. Wu, *Chem. Mater.* **19**, 634 (2007).
- ³¹X. L. Nie, S. H. Wei, and S. B. Zhang, *Phys. Rev. Lett.* **88**, 066405 (2002).
- ³²J. Vidal, F. Trani, F. Bruneval, M. A. L. Marques, and S. Botti, *Phys. Rev. Lett.* **104**, 136401 (2010).
- ³³D. O. Scanlon, A. Walsh, B. J. Morgan, G. W. Watson, D. J. Payne, and R. G. Egddell, *Phys. Rev. B* **79**, 035101 (2009).
- ³⁴J. Robertson, P. W. Peacock, M. D. Towler, and R. Needs, *Thin Solid Films* **411**, 96 (2002).
- ³⁵R. Gillen and J. Robertson, *Phys. Rev. B* **84**, 035125 (2011).
- ³⁶F. A. Benko and F. P. Koffyberg, *Mater. Res. Bull.* **21**, 753 (1986).
- ³⁷S. Mahapatra and S. A. Shivashankar, *Chem. Vap. Deposition* **9**, 238 (2003).
- ³⁸D. Shin, J. S. Foord, R. G. Egddell, and A. Walsh, *J. Appl. Phys.* **112**, 113718 (2012).
- ³⁹D. O. Scanlon and G. W. Watson, *J. Mater. Chem.* **21**, 3655 (2011).
- ⁴⁰A. Sarkar, S. Ghosh, S. Chaudhuri, and A. K. Pal, *Thin Solid Films* **204**, 255 (1991).
- ⁴¹T. Okuda, N. Jufuku, S. Hidaka, and N. Terada, *Phys. Rev. B* **72**, 144403 (2005).
- ⁴²D. Li, X. D. Fang, Z. X. Deng, W. W. Dong, R. H. Tao, S. Zhou, J. M. Wang, T. Wang, Y. P. Zhao, and X. B. Zhu, *J. Alloys Compd.* **486**, 462 (2009).
- ⁴³K. A. Vanaja, R. S. Ajimsha, A. S. Asha, and M. K. Jayaraj, *Appl. Phys. Lett.* **88**, 212103 (2006).
- ⁴⁴L. Liu, K. W. Bai, H. Gong, and P. Wu, *Phys. Rev. B* **72**, 125204 (2005).
- ⁴⁵S. H. Wei, *Comput. Mater. Sci.* **30**, 337 (2004).
- ⁴⁶D. J. Aston, D. J. Payne, A. J. H. Green, R. G. Egddell, D. S. L. Law, J. Guo, P. A. Glans, T. Learmonth, and K. E. Smith, *Phys. Rev. B* **72**, 195115 (2005).
- ⁴⁷M. V. Lalic, J. Mestnik, A. W. Carbonari, and R. N. Saxena, *Solid State Commun.* **125**, 175 (2003).
- ⁴⁸Y. F. Wang, Y. J. Gu, T. Wang, and W. Z. Shi, *J. Alloys Compd.* **509**, 5897 (2011).
- ⁴⁹B. J. Ingram, B. J. Harder, N. W. Hrabe, T. O. Mason, and K. R. Poeppelmeier, *Chem. Mater.* **16**, 5623 (2004).
- ⁵⁰Z. H. Deng, X. D. Fang, R. H. Tao, W. W. Dong, S. Zhou, G. Meng, and J. Z. Shao, *J. Alloys Compd.* **509**, 5300 (2011).